

# Pulse-shaping method for real-time neutron/gamma discrimination at low sampling rates\*

Jiaxin Li,<sup>1,2</sup> Huiliang Hou,<sup>1,2,†</sup> Yuefeng Huang,<sup>1,2</sup> Maosong Cheng,<sup>1,2</sup> and Zhimin Dai<sup>1,2,‡</sup>

<sup>1</sup>*Shanghai Institute of Applied Physics, Chinese Academy of Sciences, Shanghai 201800, China*

<sup>2</sup>*University of Chinese Academy of Sciences, Beijing 100049, China*

The NaI:Tl scintillator is an innovative material for dual-gamma-ray and neutron detection with a low  ${}^6\text{Li}$  concentration. To achieve real-time n/ $\gamma$  discrimination, a zero-crossing time comparison algorithm based on trapezoidal pulse shaping was developed. The algorithm can operate efficiently at low sampling rates and was implemented on a single-probe portable digital n/ $\gamma$  discriminator based on a field-programmable gate array (FPGA). The discriminator and NaI:Tl,  ${}^6\text{Li}$  detector were tested in a neutron-gamma mixed field produced by an  ${}^{241}\text{Am-Be}$  neutron source to evaluate the performance of the algorithm. The Figure of Merits (FoM) was measured as 2.88 at a sampling rate of 50 MHz, indicating that the discriminator with its embedded algorithm has a promising n/ $\gamma$  discrimination capability. Efficient discrimination at sampling rates of 40 and 25 MHz demonstrates that the capability of this method is not limited by low sampling rates.

Keywords: FPGA, NaI:Tl,  ${}^6\text{Li}$ , Real time, Neutron/gamma discrimination, Pulse shaping

## I. INTRODUCTION

Efficient neutron detection is in high demand in numerous fields, such as radiation monitoring[1], neutron imaging[2], and national security[3].  ${}^3\text{He}$  gaseous detectors are widely used in neutron detection systems. Although  ${}^3\text{He}$  position-sensitive detectors show excellent neutron-gamma discrimination ability, reasonable spatial resolution (1–10 mm), and high count-rate capability[4], the high cost and shortage of  ${}^3\text{He}$  limit their application. The world supply of  ${}^3\text{He}$  used to come entirely from the decay of tritium originating from nuclear weapons programs in the U.S. and Russia[5]. The mainstream choice of neutron detectors has shifted to scintillator detectors, including organic and inorganic scintillators. Because neutron emission is often accompanied by gamma rays, n/ $\gamma$  discrimination is a critical technique for neutron detection.

Scintillator detectors not only provide a high light yield and excellent energy resolution but also emit discriminative neutron pulse signals that can be extracted by pulse shape discrimination (PSD) methods[6]. Most PSD methods have been tested with plastic scintillators, such as EJ-276 and EJ-309, and most tested FoMs are better than 1.0[7–10], which means that they can extract most neutron signals from mixed neutron-gamma radiation field. Plastic scintillators are preferred over liquid scintillators because of their attractive features, including low cost, self-containment, and ease of processing [10]. Among the anthracene, stilbene, and p-terphenyl scintillators, anthracene scintillators exhibit the highest light yield and PSD performance[11]. Inorganic scintillators have been developed using  ${}^6\text{Li}(n, \alpha){}^3\text{H}$  reaction. The reasonable discrimination performance of elpasolite scintillators, such as CLYC, has been verified.[12, 13]. As the latest inorganic scintillator, NaI:Tl,  ${}^6\text{Li}$  is capable of efficient dual detection of thermal neutrons and gamma rays by doping with

${}^6\text{Li}$  while maintaining the original NaI:Tl scintillation properties. Moreover, NaI:Tl,  ${}^6\text{Li}$  scintillators can be significantly larger than CLYCs[6].

In recent years, many time- and frequency-domain methods have been proposed and compared based on different features of the output signals from scintillators[7]. For example, the charge-comparison method integrates pulse signals and calculates the charge ratio in the time domain[7], whereas the discrete wavelet transform method calculates a scaling function that represents the energy density in the frequency domain[14]. Additionally, intelligent techniques such as neural networks have been applied to PSD [9, 15]. However, many matrix operations may be required in the frequency domain and artificial intelligence methods, which are limited to offline computing[15]. Such tedious and complex algorithms require long identification times; thus, they are not superior to fast real-time analysis. A confusing problem with time-domain methods is that their PSD performance is not as satisfactory as that of intelligence methods. One approach to solving this problem involves the use of pulse shaping, which can be applied to alter the features of the output signals from scintillators. A larger difference in signal shapes leads to better PSD performance. The pulse-shaping technique can decompose and synthesize signals in real time in an FPGA[16, 17] and potentially simplify PSD methods while maintaining good PSD performance.

Several digitizer boards are used to sample signals in most traditional PSD methods; however, a host computer is required for data processing[18–20]. A possible constraint for developing a real-time discriminator without a computer is the adaptability of the PSD algorithms. Additionally, to achieve better PSD performance, some algorithms have high hardware requirements [19–24], such as high sampling rates and large FPGA logic resources. However, the device size, power consumption, and cost have also been considered in some applications[25]. This paper proposes a time-domain algorithm based on a trapezoidal shaper to achieve real-time n/ $\gamma$  discrimination and demonstrates the feasibility of deploying this algorithm in a portable FPGA-based discriminator.

The PSD performance was evaluated using a NaI:Tl,  ${}^6\text{Li}$  scintillator at low sampling rates.

\* This work was supported by the National Natural Science Foundation of China (NSFC) (grant No. 12075308)

† Corresponding author, houhuiliang@sinap.ac.cn

‡ Corresponding author, daizhimin@sinap.ac.cn

76

## II. METHOD

77

### A. Hardware design

78 A block schematic of the  $n/\gamma$  discriminator is shown in  
 79 Fig. 1(a). The  $n/\gamma$  discriminator receives signals from the  
 80 NaI:Tl: $^{6}\text{Li}$  detector and uploads the latest spectra to a com-  
 81 puter every two seconds. Most signal processing is performed  
 82 in FPGA so the analog circuit only needs to satisfy the sig-  
 83 nal amplification and noise reduction requirements. After  
 84 the neutron and gamma pulse signals are produced by the  
 85 preamplifier, they must be further amplified and adjusted in  
 86 the analog circuits of the discriminator. AD829 achieves its  
 87 230 V/ $\mu\text{s}$  uncompensated slew rate and 750 MHz gain band-  
 88 width while requiring only 5 mA of current from power sup-  
 89 plies, which is suitable for building a main amplifier. With  
 90 a low input voltage noise of 1.7 nV/ $\sqrt{\text{Hz}}$ , AD829 serves  
 91 as an input buffer for an analog-to-digital converter (ADC).  
 92 The amplified analog signals are then digitalized in a high-  
 93 speed ADC (AD9236, Analog Device), which uses a multi-  
 94 stage differential pipelined architecture to provide 12-bit res-  
 95 olution at up to 80 Msps. AD9236 operates from a single  
 96 3.3 V power supply and has a low 366 mW power consump-  
 97 tion at 80 Msps. The sample-to-hold amplifier (SHA) input  
 98 maintains excellent performance for input frequencies up to  
 99 100 MHz and is configured as single-ended in this appli-  
 100 cation. A single-ended clock input was used to control all  
 101 the internal conversion cycles provided by FPGA. A clock  
 102 duty cycle stabilizer (DCS) was used to re-time the non-  
 103 sampling edge and provide an internal clock signal with a  
 104 nominal 50% duty cycle. This allows for a wide range of  
 105 clock input duty cycles without affecting the performance of  
 106 AD9236. Hence, additional single-ended-to-differential cir-  
 107 cuits or clock sources are not required. Using an internal  
 108 reference voltage, the circuit design can be simplified. Fi-  
 109 nally, the digitalized signals were delivered to the Spartan-7  
 110 FPGA (XC7S25-1CSGA324C, Xilinx), where a critical dis-  
 111 crimination algorithm was implemented. The FPGA must  
 112 perform three main tasks: provide the clock source for the  
 113 ADC, receive and process the digitized signal from the ADC,  
 114 and upload the energy spectra. Digital circuits require volt-  
 115 ages of 1.0V, 1.8V, and 3.3V. These low voltages were gener-  
 116 ated using low-dropout (LDO) linear regulators (TLV74110,  
 117 TLV74118, TLV75533, TI). These LDO regulators have fixed  
 118 output voltages and their peripheral circuits require only ca-  
 119 pacitors for filtering.

120 The PSD algorithm was implemented using several mod-  
 121 ules on FPGA. The digital antinoise filter and signal prepro-  
 122 cessing module use FIFO to cache the data from the ADC.  
 123 Furthermore, they filter the high-frequency noise and adjust  
 124 the pulse shape when severe pulse undershoot occurs. In-  
 125 stead of being sent directly to the discrimination module, the  
 126 filtered signals are first processed using a trapezoidal pulse  
 127 shaper. The trapezoidal pulse shaper is conducive to mag-  
 128 nifying the difference between neutron and gamma signals.  
 129 Its low computational complexity makes the real-time dis-  
 130 crimination of FPGA easy to achieve. The input and output  
 131 signals of the trapezoidal shaper are processed separately in

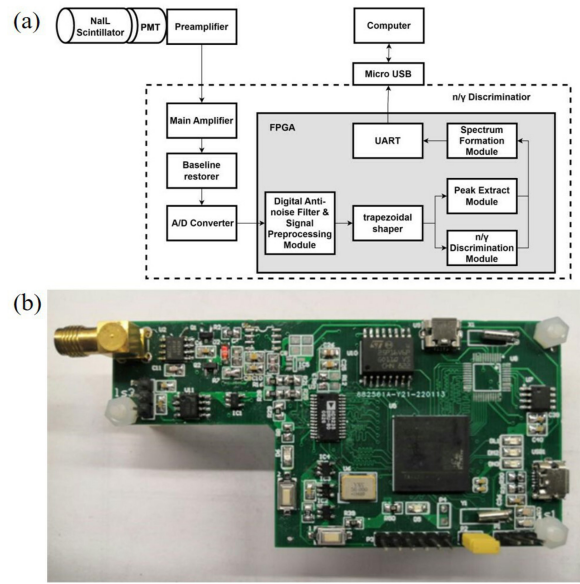


Fig. 1. (a) Block schematic of the real-time digital pulse shape dis-  
 criminator. (b) Real-time digital pulse shape discriminator.

132 two parallel modules. One module is the  $n/\gamma$  discrimination  
 133 module, which identifies signal types by analyzing the char-  
 134 acteristics of the shaped signals, and the other is the peak ex-  
 135 traction module, which selects the maximum amplitude from  
 136 the pulse data in the duration of the original signals. Conse-  
 137 quently, with the identified signal types and amplitudes, the  
 138 spectrum formation module forms gamma spectra, neutron  
 139 response spectra, and PSD plots, which are updated in real-  
 140 time after a new pulse signal arrives. Owing to the low power  
 141 consumption of the discriminator and the small amount of  
 142 spectrum data, only one USB port is required for power sup-  
 143 ply and data transmission.

### B. Pulse-shaping technique

144 In the radiation detection system, RC-CR circuits and a  
 145 Sallen-Key filter were used to filter out noise from the ampli-  
 146 fied nuclear signals to obtain an optimum signal-to-noise ratio  
 147 (SNR). These filters remove the high-frequency components  
 148 in the frequency domain, causing a change in the shape of the  
 149 signals in the time domain. For example, RC-CR circuits and  
 150 a Sallen-Key filter can process a signal into a Gaussian-like  
 151 shape in both analog and digital ways [26–28]. In addition  
 152 to filtering, the signals must be specifically shaped to accom-  
 153 modate different application scenarios. The signal should be  
 154 narrow at high count rates and have a flat top for amplitude  
 155 analysis. In time analysis, steepening the leading edge of the  
 156 signals makes the timing accurate. Using the digital pulse-  
 157 shaping technique, a digital shaper can meet diverse require-  
 158 ments and process signals into a variety of shapes, such as  
 159 trapezoidal and triangular.

160 A trapezoidal pulse-shaping algorithm was developed us-  
 161 ing the z-transform method[29]. The z-transform method

comprises two main steps. The first step is to acquire the transfer function  $H(z)$  through the z-transformation of the input and output signals. The next step is to apply an inverse z-transform to obtain the equations for the input and output signals in the time domain.

Common signal-processing algorithms, such as fast Fourier transform (FFT) and finite impulse response (FIR) filters, require numerous multiplication and addition operations. Moreover, the internal DSP slices of the FPGA can conveniently perform basic multiplication and addition operations. As shown in Fig. 2(a), the trapezoidal pulse-shaping algorithm derived from the z-transform method could be implemented as a shaper in FPGA. Because this algorithm requires high-precision multiplication and addition operations, the adders and multipliers should have large bit widths. This algorithm also requires additional operations to remove the baseline drift caused by noise accumulation [29].

Another method of achieving a digital trapezoidal shaper is the unfolding synthesis technique. Because of the limitations of the bit width, hardware resources, and real-time processing requirements, a trapezoidal shaper should be simple and efficient for FPGA. The unfolding technique was introduced to transform digital signals from an ADC into a unit impulse, which can approximately synthesize any pulse shape [17]. The nuclear signal amplitude increased rapidly to a maximum value and then decayed at a relatively slow rate. For NaI:Tl crystals, the decay time of light output has both fast and slow components [30]. The current signal output from the PMT was converted into a voltage pulse in the resistive feedback preamplifier followed by an RC network. Fig. 3(a) shows the digitalized voltage pulse, which can be expressed as:

$$V[n] = A \left( e^{-\frac{n}{\tau_1}} - e^{-\frac{n}{\tau_2}} \right), \quad (1)$$

where  $\tau_1$  and  $\tau_2$  represent the decay time constants of the digital signal in a bi-exponential shape, which includes the preamplifier time constant, scintillation fluorescence time constant, electronic characteristics of the anode, and preamplifier-anode coupling.  $A$  indicates the pulse amplitude and also controls the signal width. The interval between two adjacent sampling points  $n$  is determined by the sampling rate. Eq. (1) serves as a fitting model to obtain the decay time constants of the digital pulse.

Because the output signal of the detector has a biexponential shape, the first step is to deconvolute the biexponential signal into a unit impulse  $\delta[n]$ . The operational algorithm of a system that unfolds an exponential unit impulse response is given by the following equation[17]:

$$\delta[n] = x_N[n] - a \cdot x_N[n - 1]. \quad (2)$$

There is also a double exponential impulse-shaping algorithm for obtaining a narrower  $\delta$  signal, which might result in better anti-pile-up applications[31]. All deconvolution methods produce an approximate  $\delta$  signal that retains time and amplitude information. The difference between these methods lies in the width of the  $\delta$  signal and complexity of the algorithm. Although Eq. (2) is derived for a single exponential pulse, good shaping results can be obtained by using Eq. (2)

twice. Fig. 3(c) and Fig. 3(d) show that the signal becomes significantly narrower and smaller after two deconvolutions.

The next step was to synthesize a unit pulse using a trapezoidal pulse. The operational algorithm for the synthesis system was deduced from the shape of the target waveform. A standard trapezoidal pulse can be described as

$$y[n] = \begin{cases} \frac{A}{k} & n < k \\ A & k \leq n \leq m \\ -\frac{A}{k} \cdot n + \frac{A}{k} \cdot (2 \cdot k + l) & x > m \end{cases}. \quad (3)$$

After differentiating the primary function  $y[n]$ , the function value of each interval becomes constant, resulting in  $d[n]$

$$d[n] = \begin{cases} \frac{A}{k} & n \leq k \\ -\frac{A}{k} & m \leq n \leq j \end{cases}. \quad (4)$$

The weighted and shifted unit impulses can be used to represent the differentiation of  $y[n]$ . Therefore, an alternative expression for  $d[n]$  is as follows:

$$d[n] = \frac{A}{k} \cdot (u[n] - u[n - k]) - \frac{A}{k} \cdot (u[n - m] - u[n - j]). \quad (5)$$

$\delta[n]$  is the result of the difference operation of  $u[n]$ , and the synthesis system based on recursive difference equations in the time domain[32, 33] is given as follows:

$$p[n] = \frac{A}{k} \cdot (\delta[n] - \delta[n - k]) - \frac{A}{k} \cdot (\delta[n - m] - \delta[n - j]), \quad (6)$$

$$d[n] = p[n] + d[n - 1], \quad (7)$$

$$y[n] = d[n] + y[n - 1], \quad (8)$$

where  $k$  is the duration of the rising/falling edge of the trapezoidal pulse and  $|m - j|$  is the duration of the flat time of the trapezoidal pulse.  $|m - j|$  and  $k$  could be large enough so that the signal has enough time to rise to its maximum amplitude, thus compensating for the ballistic deficit effect[34]. However, a long signal duration causes pile-up events when the count rate is high, which is unhelpful for  $n/\gamma$  discrimination. In this study, we did not consider the pile-up situation. Thus, we can only discard pile-up events by determining whether there are multiple peaks in the pulse duration. The tail pile-up pulses could be separated when only counting was considered. However, when a neutron pulse and gamma pulse are stacked together, it is difficult to separate them while retaining their distinct original features. The challenge of separating the neutron and gamma signal pile-ups remains. Therefore, the parameters of the algorithm were set to prevent the shape of the trapezoidal signal width from exceeding the original signal width. Fig. 2(b) shows the block diagram of the trapezoidal shape algorithm. The parameter  $b$  is the amplitude factor that controls the digital gain. The parameters  $a_1$  and  $a_2$  are determined by the decay time constant  $\tau$  and sample period  $\Delta T$ :

$$a_1 = e^{-\Delta T / \tau_1}, \quad (9)$$

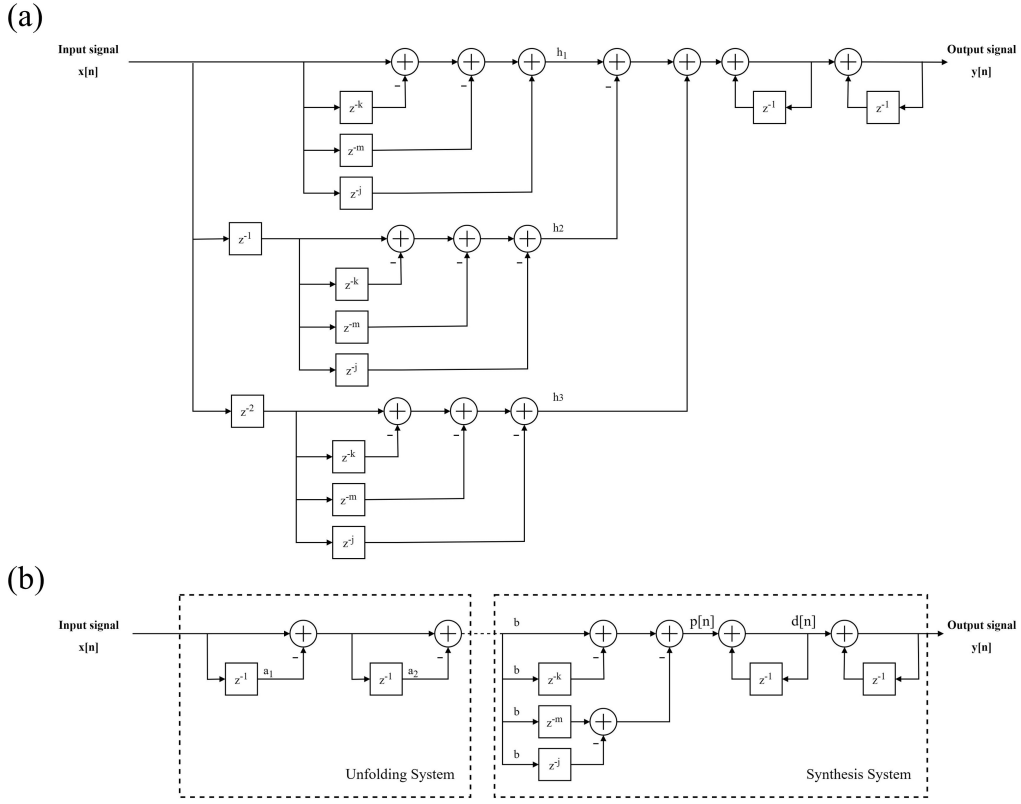


Fig. 2. (a) Functional block diagram of the trapezoidal shaper using the z-transform method. (b) Functional block diagram of the trapezoidal shaper using unfolding-synthesis technique.

$$a_2 = e^{-\Delta T/\tau_2}. \quad (10)$$

In Fig. 2, compared with the z-transform method, the trapezoidal shaper derived from the idea of unfolding synthesis technique has fewer adders and multipliers. In reality, fewer operations of the trapezoidal shaper are attributed to the deconvolution of the digital pulse. Signal deconvolution shifts the target of the trapezoidal shape from a bi-exponential signal to a  $\delta$  signal that retains the energy information of the original signal[35]. The implementation of signal deconvolution reduces baseline shifts at high count rates and improves energy resolution[35, 36]. Hence, fewer operations do not necessarily result in poor performance. The recursive method for the trapezoidal shaper using Eqs. (2), (6), (7), and (8) is shown in Fig. 2(b).

### C. PSD algorithm based on a trapezoidal shaper

The digitalized neutron and gamma signals sampled from the ADC are shown in Fig. 3(a). Neutron and gamma waveforms were normalized to the same area for comparison with the same gamma-equivalent energy. We consider the rise time as the time when a signal crosses from a specific low-voltage

threshold to a specific upper-voltage threshold (10% to 90%), and the fall time as 90% to 10% of the signal tail. The rise time of the gamma signal was 58 ns and its fall time was 470 ns. The rise and fall times of the neutron signal were 46 ns and 413 ns. The two signals in Fig. 3(a) could be fitted using a bi-exponential function. The fast component of the gamma signal was 70 ns and its slow component was 200 ns. The fast and slow components of the neutron signal were 64 ns and 160 ns. It is evident that the neutron and gamma signals have different decay time constants. The difference between the two signals appears to be small when viewed by the human eye. It can be presumed that the results obtained after integrating the signals directly will also be similar. The use of a trapezoidal shaper avoids the direct processing of similar original signals and analyzes the new features of the shaped signals. Because parameters  $a_1$  and  $a_2$  are set for gamma signals, the trapezoidal shaper does not match the neutron signals. Thus, the two types of signals formed different shapes, as shown in Fig. 3(b). The gamma signal is shaped into an approximate trapezoidal signal, whereas the output of the neutron signal has the characteristics of overshoot and undershoot owing to the unmatched parameters  $a_1$  and  $a_2$ . According to the output characteristics of the neutron signals from the trapezoidal shaper, the n/ $\gamma$  and peak extraction modules cooperate in the following states:

(1)  $t_1$  denotes the time at which the signal amplitude exceeds the baseline value. During time  $t_1$ , the maximum value of the original signals is determined through successive comparisons and recorded.

(2) The time  $t_2$  from when the signal decays to the baseline until it returns to zero is recorded.

(3) After completing the record of  $t_2$ , the peak value is sent to the spectrum formation module to identify whether the peak value belongs to the neutron response spectrum or the gamma spectrum by calculating the correlation factor  $\lambda$ :

$$\lambda = t_1/(t_1 + t_2). \quad (11)$$

$\lambda$  takes values between 0 and 1, and it characterizes the magnitude of the undershoot and the overshoot of the signal. When the neutron pulse signal width is relatively narrow, the signal decays quickly causing an undershoot and resulting in a long  $t_2$  and short  $t_1$  for peak extraction. Typically,  $\lambda$  of the neutron signal is smaller than that of the gamma signal, which means that the neutron peak is on the left side of the gamma peak in the PSD plot.

Low sampling rates affect the trapezoidal shaping results, but more importantly, they result in inaccurate measurements of  $t_1$  and  $t_2$ . Owing to the low-sampling-rate requirement of the shaper and the amplification of the difference between the neutron and gamma signals, this algorithm is characterized by its ability to work at low sampling rates compared to some mainstream algorithms[22].

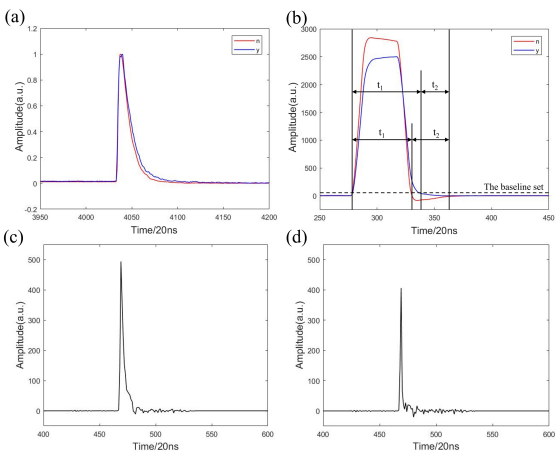


Fig. 3. (a) Averaged gamma-ray and neutron pulses from the NaI detector. (b) Illustration of the PSD algorithm based on the trapezoidal shaper. (c) First signal deconvolution of the input signal when  $a_1$  is 0.9048. (d) Second signal deconvolution of the input signal when  $a_1$  is 0.9048 and  $a_2$  is 0.7515.

The neutron and gamma signals were processed in the same trapezoidal shaper and shaped into a nonstandard trapezoidal pulse. In Fig. 3(b), although the output of the gamma signal has a relatively flat top, the output of the neutron signal has an uneven top that could shift the neutron response peak to the right in energy analysis. Thus, using the parallel-processing capabilities of the FPGA, the peak extraction module matches the peaks of the original signals to the shaped signals.

### III. EXPERIMENTAL SETUP

A  $\Phi 50.8 \text{ mm} \times 50.8 \text{ mm}$   ${}^6\text{Li}$ -enriched (95%) NaI:Tl scintillator with 1%  ${}^6\text{Li}$  doping was chosen because it has a high light output yield exceeding 30000/MeV[6]. A preliminary check of the detector response to gamma rays was performed using a  ${}^{137}\text{Cs}$  gamma source. The energy resolution was 7.01% at 662 keV. The experiments were implemented using a 30 mCi  ${}^{241}\text{Am}$ -Be neutron source. Thermal neutrons were indirectly detected through  ${}^6\text{Li}(n, \alpha){}^3\text{H}$  reaction, which emitted  ${}^3\text{H}$  and  $\alpha$  particles with a total energy of 4.79 MeV. Only part of the energy was deposited in the NaI:Tl ${}^6\text{Li}$  crystal because of the luminous efficiency of  $\alpha$  and  ${}^3\text{H}$  particles[37]. The cross section of the thermal neutron capture on  ${}^6\text{Li}$  was 940 b. A major advantage of using  ${}^6\text{Li}$  to capture neutrons is that the reaction has a high reaction energy, and a neutron response energy of 4.79 MeV can be easily distinguished from the gamma background. Additionally, discrimination between the neutron and gamma signals in the low-energy region can be avoided using the nuclear reaction method.

The count rates can differ when the distance between the  ${}^{241}\text{Am}$ -Be source and the detector varies. The count rate of gamma rays and neutrons was 1.8 kcps when the distance was set to 20 cm with a 6 mm thick lead shield, and 22 kcps without a lead shield. The  ${}^{241}\text{Am}$ -Be source was placed 20 cm away from the detector with a 6 mm thick lead shield for moderate reduction of the gamma background. Four arrangements were used to determine the appropriate PSD parameters and evaluate the pulse-shape discrimination ability of the discriminator.

The trapezoidal shaper is completed in the first part. The waveforms of digitalized signals were extracted using an integrated logic analyzer. By fitting the neutron and gamma signals with a bi-exponential function, we can obtain approximate decay time constants to build a trapezoidal shaper. After loading the original pulse data from the integrated logic analyzer into the MATLAB workspace, a shaper was built and simulated in Simulink of MATLAB. The decay time constants obtained by fitting with a biexponential function were float-point-type constants. To enhance the operation speed and save data memory in FPGA, all parameters were converted into a fixed-point type. The output results of each operation were rounded and saturated on an integer overflow because of the limitation of fixed-point precision. This is why the precision of the algorithm in FPGA decreases as the operations increase and the final shaping results are not as accurate as the theoretical calculation. An inaccurate operation output can cause a baseline shift and pulse shape distortion. The algorithm operations were most likely halted when an overflow occurred. One way to solve these problems is to control the value and bit width of the operation results and parameters, such as  $a_1$ ,  $a_2$ , and  $b$ . Because shaped signals can be observed in real time using an integrated logic analyzer, the parameters of the algorithm were manually adjusted after observation. Each adder, multiplier, and accumulator in FPGA were also set to have different output bit-width limitations.

The second part tested whether the algorithm could make signals distinctive and whether the spectrum-formation mod-

400 ule worked to form a PSD plot. The trapezoidal shaper  
 401 was implemented in the discriminator to complete the  
 402 neutron/gamma discrimination algorithm. The spectrum-  
 403 formation module in FPGA was selected to record the PSD  
 404 plot. The discriminator sampled the neutron and gamma sig-  
 405 nals for some time to acquire PSD plots, which demonstrated  
 406 different  $\lambda$  values for all counts.

407 Neutron and gamma peaks are observed in the PSD plot.  
 408 Assuming that the peaks follow a Gaussian distribution, we  
 409 use a Figure of Merit (FoM), defined as

$$410 \quad FOM = \frac{S}{FWHM_{\gamma} + FWHM_n}, \quad (12)$$

411 to determine the quality of discrimination.

412  $S$  denotes the distance between the neutron response and  
 413 gamma peaks, while  $FWHM_{\gamma}$  and  $FWHM_n$  represent the  
 414 full widths at half maximum of the corresponding peaks. The  
 415 FoM is high when there are few statistical fluctuations; the  
 416 two peaks are significantly separated, and a high FoM indi-  
 417 cates a good discrimination ability. According to the PSD  
 418 plot, the neutron signals can be distinguished if  $\lambda$  is smaller  
 419 than a threshold,  $\lambda_{standard}$ . After  $\lambda_{standard}$  was determined  
 420 and set in FPGA, the spectrum formation module was modi-  
 421 fied to form two-pulse amplitude spectra.

422 Subsequently, the determined parameters and modified  
 423 modules in FPGA were used to acquire the final spectra in the  
 424 third part. For instance, in the experiment at a 50 MHz sam-  
 425 pling rate,  $a_1 = 0.9048$ ,  $a_2 = 0.7515$ ,  $b = 1.5$ ,  $k = 10$ ,  $|m - j|$   
 426 = 20, and  $\lambda_{standard} = 0.45$ . The signals were classified as  
 427 neutron signals when  $\lambda$  was  $< 0.45$ . In this section, two 4096  
 428 channel spectra are uploaded from FPGA to a computer every  
 429 two seconds. These parameters were set manually beforehand  
 430 and could be fixed for the current experimental conditions.  
 431 Changes in the source intensity, detector type, and detector lo-  
 432 cation from the source might invalidate these parameters and  
 433 deteriorate the discrimination quality. Therefore, the experi-  
 434 mental steps described above must be repeated to obtain the  
 435 best parameters when the detection conditions change. The  
 436 fourth part is the shielding experiment conducted in the pre-  
 437 vious two parts. A 1.5 mm thick cadmium plate was used to  
 438 absorb neutrons, which allowed us to compare the discrimi-  
 439 nation efficiency and ensure that only a few neutron signals  
 440 were omitted.

#### 441 IV. RESULTS AND DISCUSSION

442 As discussed previously, a PSD discriminator and its em-  
 443 bedded algorithm were designed and implemented. With-  
 444 out lead shielding, several input and output signals from the  
 445 trapezoidal shaper were captured using an integrated logic an-  
 446 alyzer. With 6 mm lead shielding, the probability of pile-up  
 447 events occurring was reduced. The presence of massive low-  
 448 energy gamma rays results in many low-amplitude pulses, as  
 449 shown in Fig. 4(a). The signal shapes, with pulse widths  
 450 shorter than 2  $\mu$ s, are shown in Fig. 4(b). A gamma sig-  
 451 nal with a large amplitude was deliberately acquired. Af-  
 452 ter trapezoidal shaping, the gamma signals feature a flat top,

453 whereas the neutron signals exhibit an overshoot at the top.  
 454 The gamma and neutron signals exhibit small and severe un-  
 455 dershorts, respectively. Thus, a signal with an amplitude of  
 456 2836 can be identified as a neutron signal by the evident over-  
 457 shoot and undershoot. In Fig. 4(a), the neutron signal has a mi-  
 458 nor undershoot before pulse shaping. This can be eliminated  
 459 by an analog circuit of pole-zero cancellation, which was not  
 460 used in this experiment, considering the remaining original  
 461 difference in the output signals of NaI:Tl and  $^6$ Li detectors.  
 462 The fast decay of the neutron signal causes a baseline drift  
 463 in the signal after the neutron signal. However, in Fig. 4(b),  
 464 the neutron signal is restored to the baseline relatively quickly  
 465 after pulse shaping. The signal after the neutron signal was  
 466 less affected by the baseline drift. This demonstrates the abil-  
 467 ity of the pulse-shaping technique to achieve pile-up decom-  
 468 position. Fast shapers can shorten the rise and fall times of  
 469 signals, reducing the occurrence of tail pile-up events. The  
 470 shaped-signal width can be narrowed by adjusting the param-  
 471 eters of the trapezoidal shaper or using a cusp shaper. For  
 472 example, a flat top can be eliminated when  $|m - j|$  is set to  
 473 zero, and the signal is processed into a triangular shape with  
 474 a short signal width.

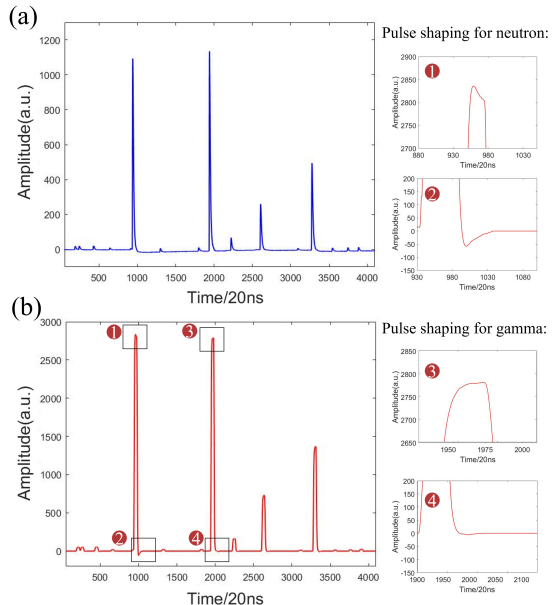


Fig. 4. (a) Amplified signals from the NaI:L detector. (b) Pulse shaping of mixed neutron-gamma signals.

476 The quality of discrimination using the pulse-shaping  
 477 method with the NaI:Tl $^6$ Li detector is shown in Fig. 5. These  
 478 plots were uploaded directly to the FPGA. The distribution  
 479 of counts with a correlation factor  $\lambda$  approximates a Gaus-  
 480 sian distribution, and there is a wide gap between the two  
 481 peaks. The left peak is the neutron response peak, whereas  
 482 the right peak is the gamma peak due to the large number  
 483 of low-energy gamma rays. The left peak disappeared af-  
 484 ter adding a 1.5 mm thick cadmium plate, proving that the

left peak was a neutron response peak. The right peak was taller in Fig. 5(b) than in Fig. 5(a), which also implies that cadmium has a high  $(n, \gamma)$  reaction cross section[38] and accordingly produces more gamma rays. Setting a threshold of 50 allowed an energy measurement from 57.195 keV to 5.695 MeV, which covered the energy range of the neutron response. Additionally, setting a threshold taller than 0 helps filter out unconcerned low-amplitude noise. In one minute, the FoM is 2.88 at a 50 MHz sampling rate allowing for the determination of the sound parameters, which is sufficient for efficiently separating the neutron and gamma signals. This effective separation was attributed to the unique shape difference between the gamma and neutron pulses amplified by the trapezoidal shaper.

Moreover, the signals can be discriminated at lower sampling rates using suitable parameters. We set  $a_1$  to 0.8825,  $a_2$  to 0.6997, and  $\lambda_{\text{standard}}$  to 0.45 for a sampling rate of 40 MHz. We set  $a_1$  to 0.8187,  $a_2$  to 0.5647, and  $\lambda_{\text{standard}}$  to 0.4 for a sampling rate of 25 MHz. The width of the trapezoidal pulse remained constant. An increase or decrease in the sampling rate did not affect the inherent decay time of the signal. From Eq. (9) and Eq. (10), we deduce that changes in the sampling rate affect  $a_1$  and  $a_2$ , and alter the results of the trapezoidal shaper. The fall time of the neutron signal was 413 ns, and there were no more than 24 sampling points on the falling edge when the sampling rate was 50 MHz. After the sampling rate was reduced to 25 MHz, there were no more than 12 sampling points at the falling edge of the neutron signal. Similarly, there were fewer than three sampling points at the rising edge. Sometimes, only one sampling point was observed during the signal rise time. Thus, owing to the short duration of a nuclear signal, a low sampling rate affects the fidelity of digitalized signals. Although the trapezoidal shaper still operates normally at a 25 MHz sampling rate, the number of sampling points available for calculating  $\lambda$  is reduced by half at a 25 MHz sampling rate compared to a 50 MHz sampling rate, which makes  $\lambda$  less accurate. As shown in Fig. 5(e), the inaccuracy of  $\lambda$  broadens the bottom of the peak and increases the distance between the two peaks. The dispersion of the counts makes the FWHM narrower. Therefore, the FoM values calculated using Eq. 12 are higher. The results show great discrimination ability at lower sampling rates when only counting is considered, but the quantization error caused at a 25 MHz sampling rate could deteriorate the energy measurements. Therefore, peak extraction should be applied to the original or output signals of the other shapers.

The sampling rate is not the main factor affecting the FoM value but a constraint of the pulse discrimination method. In some methods, the scale of the sampling rate has certain requirements for computational accuracy. The adaptability of the method described above allows discrimination over a wide range of sampling rates. The parameter selection of the trapezoidal shaper largely determines the discrimination performance of the method. The decay time constants of the output signals of the different detectors were not the same. Therefore, this pulse-shaping method must fit the digitalized signals of the ADC in advance to obtain the approximate decay time constants.

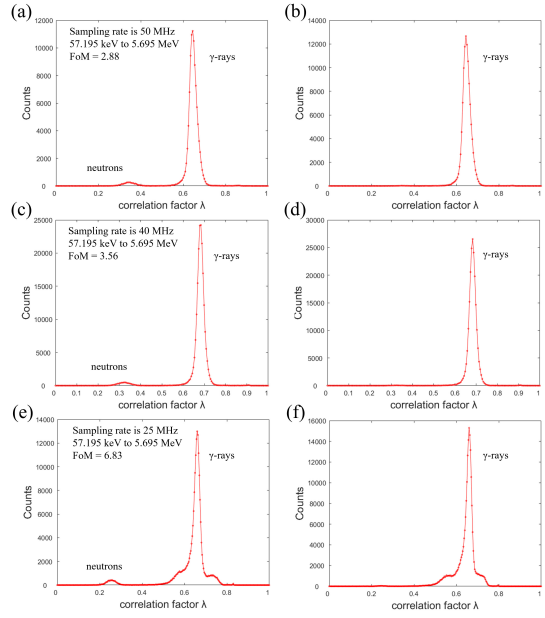


Fig. 5. PSD plot obtained at a 50 MHz sampling rate (a) without and (b) with cadmium shielding. PSD plot obtained at a 40 MHz sampling rate (c) without and (d) with cadmium shielding. PSD plot obtained at a 25 MHz sampling rate (e) without and (f) with cadmium shielding.

The neutrons emitted by the  $^{241}\text{Am}$ -Be source were not monoenergetic. The main reason why the neutron spectrum is continuous is the continuous energy of  $\alpha$  particles produced by the  $\alpha$  decay of  $^{241}\text{Am}$ [39]. Additionally, the energy loss of  $\alpha$  particles exists owing to the collisions of  $\alpha$  particles with target nuclei and Coulomb repulsion interaction. Nevertheless, the reaction products directly transitions from the excited state to the ground state and the energy transferred to the reaction products is uniquely determined. The total energy of 4.79 MeV emitted from  $^6\text{Li}(n, \alpha)^3\text{H}$  reaction is carried by  $^3\text{H}$  and  $\alpha$  particles, when the kinetic energy of the neutrons is neglected. This energy is the response of thermal neutrons and thus should exhibit a single-peak distribution at the energy of 4.79 MeV in the energy spectrum. For different scintillators, the luminous efficiencies of  $^3\text{H}$  and  $\alpha$  particles were different for the different scintillators. In this experiment, the response energy deposited in the NaI:Tl/ $^6\text{Li}$  detector was assumed to be less than 4.79 MeV.

Before implementing the PSD algorithm, we plotted Fig. 6(a) and Fig. 6(b) based on the mixed neutron-gamma radiation field for a measurement time of two minutes. The gamma-ray peak with the highest energy is the full energy peak of 4.438 MeV emitted from the  $^9\text{Be}(\alpha, n)^{12}\text{C}^*$  reaction[40]. Subsequently, a single-escape peak occurred at 3.927 MeV and a double-escape peak occurred at 3.416 MeV. The  $^{241}\text{Am}$ -Be neutron source was surrounded by boron-containing polyethylene plates that were used to prevent neutron leakage. Therefore, neutrons are captured by hydrogen in boron-containing polyethylene, which leads to a gamma-ray peak at an energy of 2.23 MeV. Moreover,  $^{10}\text{B}$  is a suitable

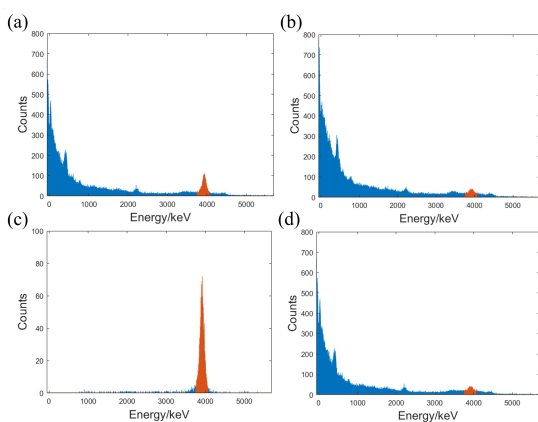


Fig. 6. Response spectrum of mixed neutron and gamma signals not using the PSD algorithm (a) without and (b) with cadmium shielding. (c) Neutron response spectrum and (d) gamma spectrum obtained using the PSD algorithm without cadmium shielding.

spectrum indicates that neutron signals with different amplitudes can be discriminated. Although the pulse width increased with the pulse amplitude, the pulse amplitude did not affect the intrinsic decay time constant. Accordingly, changes in the signal amplitude do not affect the recognition of the neutron signals. The separated gamma-energy spectra shown in Fig. 6(d) are similar to those in Fig. 6(b), but the counts will be higher in low-energy areas with cadmium shielding owing to the  $^{113}\text{Cd}(n, \gamma)$  reaction. Then, we compare the red peak area in the four spectra, which is the energy range from 3.75 MeV to 4.07 MeV. The total counts in the energy range with the gamma and neutron signals in Fig. 6(c) are 9987, and the counts reduce to 4903 when neutrons are shielded by cadmium. The peak areas of Fig. 6(c) and Fig. 6(d) are 5149 and 4755, respectively. Their sum corresponds to the total counts of the spectrum in Fig. 6(a), which indicates that the pulse-shaping method does not cause significant count loss.

## V. CONCLUSION

A portable  $n/\gamma$  discriminator and its embedded algorithm were tested at low sampling rates. The results showed satisfactory PSD performances of the NaI:Tl,  $^6\text{Li}$  scintillator and discriminator. This method can also be used for other gamma-ray and neutron dual-detection scintillators, such as CLYC and CLLB. Unlike sophisticated computer-based PSD methods, the low cost, low sampling rate, and real-time processing have significant advantages in practical applications. Future investigations into the application of this simple but robust discrimination method to the assembly of scintillator array and SiPM array are of particular interest. In radiation imaging applications, using  $n/\gamma$  dual-detection scintillator arrays with this method can simultaneously and effectively obtain neutron and gamma images, thereby reducing the size and cost of the imaging instruments.

- 
- [1] F. Zhang, Q. Zhang, R.P. Gardner et al., Quantitative monitoring of  $\text{CO}_2$  sequestration using thermal neutron detection technique in heavy oil reservoirs. *Int. J. Greenh. Gas. Con.* **79**, 154–164 (2018). doi:[10.1016/j.ijgge.2018.10.003](https://doi.org/10.1016/j.ijgge.2018.10.003)
- [2] C. Lynde, C. Frangville, R. Woo et al., On the use of pixelated plastic scintillator and silicon photomultipliers array for coded aperture gamma-neutron imaging. *IEEE Trans. Nucl. Sci.* **69**, 731–737 (2022). doi:[10.1109/TNS.2022.3140601](https://doi.org/10.1109/TNS.2022.3140601)
- [3] D. Vanderwerken, M. Millett, T. Wilson et al., Meteorologically driven neutron background prediction for homeland security. *IEEE Trans. Nucl. Sci.* **65**, 1187–1195 (2018). doi:[10.1109/TNS.2018.2821630](https://doi.org/10.1109/TNS.2018.2821630)
- [4] R.T. Kouzes n, A.T. LinterEUR, E.R. Siciliano, Progress in alternative neutron detection to address the helium-3 shortage. *Nucl. Instrum. Meth. A* **853**, 27–35 (2017). doi:[10.1016/j.nima.2017.02.022](https://doi.org/10.1016/j.nima.2017.02.022)
- [5] C.L. Wang, L.L. Funk, R.A. Riedel et al., Improved neutron-gamma discrimination for a  $^3\text{He}$  neutron detector using subspace learning methods. *Nucl. Instrum. Meth. A* **784**, 172–175 (2015). doi:[10.1016/j.nima.2014.10.046](https://doi.org/10.1016/j.nima.2014.10.046)
- [6] K. Yang, P.R. Menge, V. Ouspenski, Li co-doped NaI:TL (NaI(L)-a large volume neutron-gamma scintillator with exceptional pulse shape discrimination. *IEEE Trans. Nucl. Sci.* **64**, 2406–2413 (2017). doi:[10.1109/TNS.2017.2721398](https://doi.org/10.1109/TNS.2017.2721398)
- [7] Z. Zuo, Y.L. Xiao, Z.F. Liu et al., Discrimination of neutrons and gamma-rays in plastic scintillator based on falling-edge percentage slope method. *Nucl. Instrum. Meth. A* **1010**, 165483 (2021). doi:[10.1016/j.nima.2021.165483](https://doi.org/10.1016/j.nima.2021.165483)
- [8] E.V. Ryabeva, I.V. Urupa, E.E. Lupar et al., Calibration of EJ-276 plastic scintillator for neutron-gamma pulse shape discrimination experiments. *Nucl. Instrum. Meth. A* **1010**, 165495 (2021). doi:[10.1016/j.nima.2021.165495](https://doi.org/10.1016/j.nima.2021.165495)
- [9] H.R. Liu, Y.X. Cheng, Z. Zuo et al. Discrimination of neutrons and gamma-rays in plastic scintillator based on pulse coupled neural network. *Nucl. Sci. Tech.* **8**, 82 (2021) doi:[10.1007/s41365-021-00915-w](https://doi.org/10.1007/s41365-021-00915-w)
- [10] X. Pang, Z. Zhang, J. Zhang et al., A compact MPPC-based camera for omnidirectional ( $4\pi$ ) fast-neutron imaging based on double neutron-proton elastic scattering. *Nucl. Instrum. Meth. A* **944**, 162471 (2019). doi:[10.1016/j.nima.2019.162471](https://doi.org/10.1016/j.nima.2019.162471)

- 659 [11] T. Yanagida, K. Watanabe, Y. Fujimoto, Comparative study  
660 of neutron and gamma-ray pulse shape discrimination of an-  
661 thracene, stilbene, and p-terphenyl. Nucl. Instrum. Meth. A  
662 **784**, 111–114 (2015). doi:[10.1016/j.nima.2014.12.031](https://doi.org/10.1016/j.nima.2014.12.031)
- 663 [12] X. Wen, A. Enqvist, Pulse shape discrimination of  
664  $\text{Cs}_2\text{LiYCl}_6:\text{Ce}^{3+}$  detectors at high count rate based on  
665 triangular and trapezoidal filters. Nucl. Instrum. Meth. A **866**,  
666 129–133 (2017). doi:[10.1016/j.nima.2017.06.007](https://doi.org/10.1016/j.nima.2017.06.007)
- 667 [13] K. Li, X. Zhang, Q. Gui, et al. Characterization of the new  
668 scintillator  $\text{Cs}_2\text{LiYCl}_6:\text{Ce}^{3+}$ . Nucl. Sci. Tech. **29**, 11 (2018)  
669 doi:[10.1007/s41365-017-0342-4](https://doi.org/10.1007/s41365-017-0342-4)
- 670 [14] H. Singh, R. Mehra, Discrete wavelet transform method for  
671 high flux n- $\gamma$  discrimination with liquid scintillators. IEEE  
672 Trans. Nucl. Sci. **64**, 7 (2017). doi:[10.1109/TNS.2017.2708602](https://doi.org/10.1109/TNS.2017.2708602)
- 673 [15] H.R. Liu, Z. Zuo, P. Li et al., Anti-noise performance of  
674 the pulse coupled neural network applied in discrimination  
675 of neutron and gamma-ray. Nucl. Sci. Tech. **33**, 75 (2022).  
676 doi:[10.1007/s41365-022-01054-6](https://doi.org/10.1007/s41365-022-01054-6)
- 677 [16] V. T. Jordanov, K.V. Jordanova, Unfolding-synthesis technique  
678 for digitalpulse processing, Nucl. Instrum. Meth. A **1004**,  
679 167421 (2022). doi:[10.1016/j.nima.2022.167421](https://doi.org/10.1016/j.nima.2022.167421)
- 680 [17] V. T. Jordanov, Unfolding-synthesis technique for digital pulse  
681 processing, part 1: Unfolding. Nucl. Instrum. Meth. A **805**, 63–  
682 71 (2016). doi:[10.1016/j.nima.2015.07.040](https://doi.org/10.1016/j.nima.2015.07.040)
- 683 [18] B. Blair, C. Chen, A. Glenn et al., Gaussian mixture models  
684 as automated particle classifiers for fast neutron detectors. Stat.  
685 Anal. Data Min. **12**, 479–488 (2019). doi:[10.1002/sam.11432](https://doi.org/10.1002/sam.11432)
- 686 [19] S. Qi, J. Li, S. Wang et al., Online neutron/gamma discrimi-  
687 nation and source detection using CLYC(Ce) scintillator: A  
688 sequential approach. Nucl. Instrum. Meth. A **1014**, 165733  
689 (2021). doi:[10.1016/j.nima.2021.165733](https://doi.org/10.1016/j.nima.2021.165733)
- 690 [20] N. Cruz, B. Santos, A. Fernandes et al., The Design and Per-  
691 formance of the Real-Time Software Architecture for the ITER  
692 Radial Neutron Camera. IEEE Trans. Nucl. Sci. **66**, 7 1310–  
693 1317(2019) doi:[10.1109/TNS.2019.2907056](https://doi.org/10.1109/TNS.2019.2907056)
- 694 [21] A. Fernandes, N. Cruz, B. Santos et al., FPGA Code for the  
695 Data Acquisition and Real-Time Processing Prototype of the  
696 ITER Radial Neutron Camera. IEEE Trans. Nucl. Sci. **66**, 7  
697 1318–1323(2019) doi:[10.1109/TNS.2019.2903646](https://doi.org/10.1109/TNS.2019.2903646)
- 698 [22] V.T. Jordanov, Pile up real time pulse shape discrimination  
699 based on ballistic deficit measurement and digital time invari-  
700 ant pulse shaping. 2018 IEEE Nuclear Science Symposium and  
701 Medical Imaging Conference (NSS/MIC), Sydney, Australia  
702 10-17 November 2018. doi:[10.1109/NSSMIC.2018.8824502](https://doi.org/10.1109/NSSMIC.2018.8824502)
- 703 [23] M. Nakhostin, Digital discrimination of neutrons and  $\gamma$ -rays  
704 in liquidscintillation detectors by using low sampling fre-  
705 quency ADCs. Nucl. Instrum. Meth. A **916**, 66–70 (2019).  
706 doi:[10.1016/j.nima.2018.11.021](https://doi.org/10.1016/j.nima.2018.11.021)
- 707 [24] J. Zhang, M.E. Moore, Z. Wang et al., Study of sampling rate  
708 influence on neutron-gamma discrimination with stilbene cou-  
709 pled to a silicon photomultiplier. Appl. Radiat. Isot. **128**, 120–  
710 124 (2017). doi:[10.1016/j.apradiso.2017.06.036](https://doi.org/10.1016/j.apradiso.2017.06.036)
- 711 [25] J. Cai, D. Li, P. Wang, et al. Fast pulse sampling module for  
712 real-time neutron-gamma discrimination. Nucl. Sci. Tech. **30**,  
713 84 (2019) doi:[10.1007/s41365-019-0595-1](https://doi.org/10.1007/s41365-019-0595-1)
- 714 [26] J. Zhou, W. Zhou, H. Xu, Improvement of digital S-K filter and  
715 its application in nuclear signal processing. Nucl. Sci. Tech. **24**,  
716 060401 (2013) doi:[10.13538/j.1001-8042/nst.2013.06.020](https://doi.org/10.13538/j.1001-8042/nst.2013.06.020)
- 717 [27] J. Zhou, W. Zhou, J. Lei et al., Study of time-domain digital  
718 pulse shaping algorithms for nuclear signals. Nucl. Sci. Tech.  
719 **23**, 150–155 (2012) doi:[10.13538/j.1001-8042/nst.23.150-155](https://doi.org/10.13538/j.1001-8042/nst.23.150-155)
- 720 [28] Q. GE, L. GE, H. YUAN, et al. A new digital Gaus-  
721 sian pulse shaping algorithm based on bilinear transfor-  
722 mation. Nucl. Sci. Tech. **26**, 010402 (2015) doi:[10.13538/j.1001-8042/nst.26.010402](https://doi.org/10.13538/j.1001-8042/nst.26.010402)
- 723 [29] X. Hong, Y. Ma, J. Zhou et al., New methods to remove base-  
724 line drift in trapezoidal pulse shaping. Nucl. Sci. Tech. **26**,  
725 050402 (2015) doi:[10.13538/j.1001-8042/nst.26.050402](https://doi.org/10.13538/j.1001-8042/nst.26.050402)
- 726 [30] W. Xiao, A.T. Farsoni, H.Yang et al., A new pulse model for  
727 NaI(Tl) detection systems. Nucl. Instrum. Meth. A **763**, 170–  
728 173 (2014). doi:[10.1016/j.nima.2014.06.022](https://doi.org/10.1016/j.nima.2014.06.022)
- 729 [31] Y. Liu, M. Wang, W. Wan et al., Counting-loss cor-  
730 rectation method based on dual-exponential impulse  
731 shaping. J Synchrotron Radiat. **27**, 1609–1613 (2020)  
732 doi:[10.1107/S1600577520010954](https://doi.org/10.1107/S1600577520010954)
- 733 [32] J. Lanchares, O. Garnica,J.L. Risco-Martín et al., Real-  
734 time evolvable pulse shaper for radiation measure-  
735 ments. Nucl. Instrum. Meth. A **727**, 73–83 (2013).  
736 doi:[10.1016/j.nima.2013.05.164](https://doi.org/10.1016/j.nima.2013.05.164)
- 737 [33] J. Liu, J. Yang, G. Zeng, et al., Implementation of a cusp-like  
738 for real-time digital pulse shaper in nuclear spectrometry. Nucl.  
739 Sci. Tech. **28**, 103 (2017) doi:[10.1007/s41365-017-0248-1](https://doi.org/10.1007/s41365-017-0248-1)
- 740 [34] V.T. Jordanov, G.F. Knoll, Digital synthesis of pulse shapes  
741 in real time for high resolution radiation spectroscopy. Nucl.  
742 Instrum. Meth. A **345**, 337–345 (1994). doi:[10.1016/0168-9002\(94\)91011-1](https://doi.org/10.1016/0168-9002(94)91011-1)
- 743 [35] S. Saxena, A. I. Hawari, Digital pulse deconvolution with  
744 adaptive shaping for real-time high-resolution high-throughput  
745 gamma spectroscopy. Nucl. Instrum. Meth. A **954**, 161288  
746 (2020). doi:[10.1016/j.nima.2018.09.123](https://doi.org/10.1016/j.nima.2018.09.123)
- 747 [36] X. Wang, J. Zhou, M. Wang et al., Signal modeling and impulse  
748 response shaping for semiconductor detectors. Nucl. Sci. Tech.  
749 **33**, 4 (2021) doi:[10.1007/s41365-022-01027-9](https://doi.org/10.1007/s41365-022-01027-9)
- 750 [37] D. Ponomarev, D. Filosofov, J. Khushvaktov et al., NaI(Tl+Li)  
751 scintillator as multirange energies neutron detector. JINST **16**,  
752 P12011 (2021). doi:[10.1088/1748-0221/16/12/P12011](https://doi.org/10.1088/1748-0221/16/12/P12011)
- 753 [38] G. Rusev, M. Jandel, M. Krtička et al., Cascade  $\gamma$  rays fol-  
754 lowing capture of thermal neutrons on  $^{113}\text{Cd}$ . Phys. Rev. C **88**,  
755 057602 (2013) doi:[10.1103/PhysRevC.88.057602](https://doi.org/10.1103/PhysRevC.88.057602)
- 756 [39] J. Scherzinger, J.R.M. Annand, G. Davatz et al., Tagging fast  
757 neutrons from an  $^{241}\text{Am}/^9\text{Be}$  source, Appl. Radiat. Isot. **98**,  
758 74–79 (2015) doi:[10.1016/j.apradiso.2015.01.003](https://doi.org/10.1016/j.apradiso.2015.01.003)
- 759 [40] S. Croft, The use of neutron intensity calibrated  $^9\text{Be}(\alpha,$   
760 n) sources as 4438 keV gamma-ray references standards,  
761 Nucl. Instrum. Methods Phys. Res. A **281**, 103–116 (1989)  
762 doi:[10.1016/0168-9002\(89\)91221-7](https://doi.org/10.1016/0168-9002(89)91221-7)